Lawrence Berkeley National Laboratory
LBL Publications

Title
Lessons learned from FeSb2O4 on stereoactive lone pairs as a design principle for anion insertion

Permalink
https://escholarship.org/uc/item/936893qp

Journal
Cell Reports Physical Science, 2(10)

ISSN
2666-3864

Authors

Zaheer, Wasif
Agbeworvi, George
Perez-Beltran, Saul
et al.

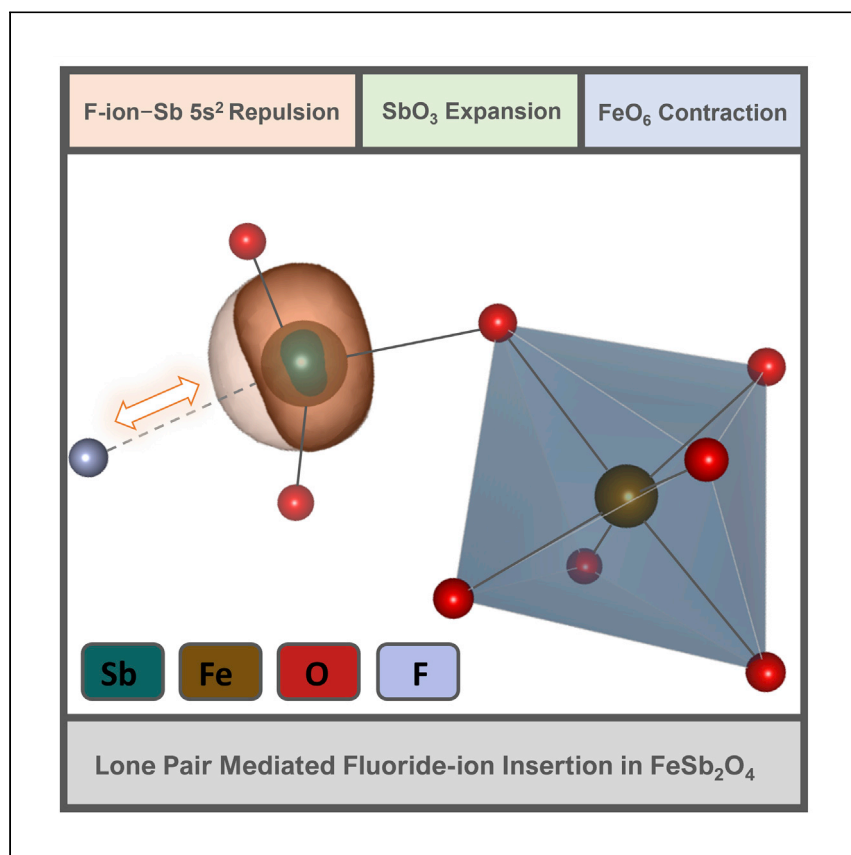Publication Date
2021-10-01

DOI
10.1016/j.xcrp.2021.100592

Peer reviewed

Article

Lessons learned from $FeSb_2O_4$ on stereoactive lone pairs as a design principle for anion insertion

| F-ion–Sb $5s^2$ Repulsion | SbO_3 Expansion | FeO_6 Contraction |

Sb · Fe · O · F

Lone Pair Mediated Fluoride-ion Insertion in $FeSb_2O_4$

Wasif Zaheer, George Agbeworvi, Saul Perez-Beltran, ..., Jinghua Guo, David Prendergast, Sarbajit Banerjee

banerjee@chem.tamu.edu

Highlights

Topochemical insertion of fluoride ions is mediated by synergies between Fe and Sb centers

p-block electron lone pairs weaken anion-lattice interactions

X-ray ptychography imaging demonstrates bulk fluoride-ion diffusion

Sb $5s^2$ electron lone pairs enable fluoride-ion deinsertion and facile diffusion

Despite several decades of research, fundamental design principles for anion insertion in crystalline lattices remain poorly explored. Zaheer et al. provide a fundamental design principle based on electronic structure considerations that allows use of anions (fluoride ions) instead of cations for electrochemical energy storage.

Article

Lessons learned from $FeSb_2O_4$ on stereoactive lone pairs as a design principle for anion insertion

Wasif Zaheer,[1,2,3] George Agbeworvi,[1] Saul Perez-Beltran,[1] Justin L. Andrews,[1] Yierpan Aierken,[3]
Conan Weiland,[4] Cherno Jaye,[4] Young-Sang Yu,[2] David A. Shapiro,[2] Sirine C. Fakra,[2]
Daniel A. Fischer,[4] Jinghua Guo,[2] David Prendergast,[3] and Sarbajit Banerjee[1,5,6,]*

SUMMARY

Fluoride-ion batteries are an attractive energy storage concept analogous to lithium-ion batteries but feature an inverted paradigm where anions are the principal charge carriers. Insertion hosts that can reversibly insert fluoride ions at room temperature are exceedingly sparse. Here, we report that topochemical insertion of fluoride ions in $FeSb_2O_4$ involves Fe^{2+}/Fe^{3+} redox but is mediated by multicenter synergies between iron and antimony centers. Separation of the redox center from the p-block coordination site alleviates structural strain by enabling compensatory contraction and expansion of FeO_6 and SbO_3 polyhedra, respectively. p-block electron lone pairs play a critical role in weakening anion-lattice interactions, enabling reversible fluoride-ion diffusion across microns. The results illuminate the key principle that interactions traceable to stereoactive lone pairs can be used to mediate anion-lattice interactions and suggest that anion insertion hosts can be designed by pairing redox-active transition metals with p-block cations bearing stereochemically active electron lone pairs.

INTRODUCTION

As the fuel mixes of energy grids worldwide trend decidedly greener, and with an increasing drive toward electromobility to mitigate the catastrophic effects of fossil fuels on the climate, there is an urgent need to diversify the range of viable electrochemical energy storage technologies.[1,2] Although Li-ion energy storage technologies are currently the dominant paradigm,[2–5] realizing the full potential of renewable energy technologies and meeting the challenging performance requirements of electromobility and large-area storage at different scales and formats will require a myriad of energy storage options spanning the range from flow batteries to "beyond Li-ion" technologies.[2–5] Materials criticality is a particular concern, given the limited earth abundance and accessibility of elements such as lithium and cobalt, which are the mainstays of current battery technologies.[6] Supplanting lithium with other monovalent (e.g., Na^+ and K^+) and multivalent ions (e.g., Mg^{2+}, Ca^{2+}, and Al^{3+}) has prospects for increased sustainability, improved performance, greater economic viability of large-area formats, and, potentially, improved safety.[3,4,6–9] Much recent attention has focused on elucidating design principles for multivalent cation diffusion and has led to ideas such as frustrated coordination, desolvation at interfaces, the softness of the host lattice, and polaron diffusion.[3,7–9] An intriguing alternative paradigm can be envisioned based on reversible shuttling of anions. As the smallest anions with a Shannon radius of 1.33 Å, fluoride ions have attracted the most attention. However, fluoride-ion energy storage constructs typically involve

[1]Department of Chemistry and Department of Material Science and Engineering, Texas A&M University, College Station, TX 77845-3012, USA

[2]Advanced Light Source, Lawrence Berkeley National Laboratory, 1 Cyclotron Road, Berkeley, CA 94720, USA

[3]The Molecular Foundry, Lawrence Berkeley National Laboratory, Berkeley, CA 94720, USA

[4]Material Measurement Laboratory, National Institute of Standards and Technology, Gaithersburg, MD 20899, USA

[5]Lead contact

[6]Twitter: @SarbajitBanerj1

*Correspondence: banerjee@chem.tamu.edu

https://doi.org/10.1016/j.xcrp.2021.100592

metathesis reactions.[10,11] Although such conversion reactions are conceptually attractive, given their large theoretical capacities, they are plagued in practice by the high overpotentials required to drive fluoridation of metal electrodes, the instability of metals in electrolytes, the propensity of metals to undergo parasitic reactions, and the substantial volume change resulting from conversion of a metal to its fluoride.[10–14] Fluoride-ion conversion processes are furthermore limited by challenges in diffusing the relatively large anion across passivating oxide and fluoride layers, which often limits fluoride ion mobility to surficial diffusion.[15] In the absence of well-defined interstitial sites, conversion reactions are initiated at particle surfaces and must propagate through movement of a reaction-diffusion front. At room temperature, fluoride-ion diffusion is typically limited to a few nanometers on surfaces; thus, the interiors of electrodes remain almost entirely inaccessible.[11–13,15]

Relatively less attention has been devoted to fluoride-ion insertion electrodes that are analogous to Li-ion insertion electrodes in terms of operating principles but with an inverted paradigm of redox reactions. Cathodes based on Mn^{3+}/Mn^{5+} redox have been explored in the $LaSrMnO_4/LaSrMnO_4F_2$ system and afford a theoretical capacity as high as 172 mAh/g but are nevertheless plagued by poor reversibility and parasitic reactions.[16] Co^{2+}/Co^{3+} redox underpins the La_2CoO_4/La_2CoO_4F system, which delivers a reversible capacity of 72 mAh/g. Insertion anodes have been proposed recently based on electrodes with the composition Ca_2N and Y_2N, where insertion of a fluoride ion releases an electron.[17,18] In the absence of suitable electrolytes, investigation of fluoride-ion insertion and deinsertion has required use of solid-state electrolytes, necessitating high temperatures (>160°C) and severely constraining exploration of potential intercalation hosts.[16] Bashian et al.[19] have reported partially reversible fluoride-ion insertion in ReO_3 from a liquid electrolyte. We have shown unprecedented reversible topochemical fluoride-ion insertion at room temperature within quasi-1D tunnels of $FeSb_2O_4$.[20] Topochemical insertion of fluoride ions in $FeSb_2O_4$ was accomplished by use of XeF_2, yielding nearly quantitative oxidation of divalent iron sites. Solution-phase fluoride-ion deinsertion was achieved by reaction with n-butyllithium (n-BuLi) in hexanes. The observed facile accessibility of Fe^{2+}/Fe^{3+} redox states, reversibility of fluoride-ion insertion, and bulk fluoride-ion diffusion at room temperature accessible within $FeSb_2O_4$ makes it a useful model system for elucidating mechanistic design principles. The role of the distinctive electronic structure of this compound and the synergistic effects of iron and antimony sites in facilitating reversible fluoride-ion insertion remain unexplored. We reveal here the critical importance of stereoactive lone pairs of Sb^{3+} cations in enabling facile Fe^{2+}/Fe^{3+} redox and facilitating reversibility of fluoride ion binding, providing an important design consideration for discovery of F-ion (fluoride-ion) insertion hosts.

The $[Kr]4d^{10}5s^2$ electronic configuration of trivalent antimony cations implies the presence of a stereoactive lone pair of electrons that are projected into the tunnels of $FeSb_2O_4$. Stereochemically active electron lone pairs from p-block cations can bring about pronounced structural distortions and give rise to electronic states that lie high in the valence band, where they are available for interactions with surface-adsorbed or intercalated species.[21–25] In this study, we probe the electronic structure of $FeSb_2O_4$ and its modulation upon fluoride-ion insertion using energy-variant hard X-ray photoemission spectroscopy (HAXPES) in conjunction with X-ray absorption near-edge structure (XANES) spectroscopy, scanning transmission X-ray microscopy (STXM), high-resolution X-ray ptychography, magnetic susceptibility measurements, and first-principles density functional theory (DFT) calculations along with crystal orbital Hamiltonian population (COHP) analysis. We demonstrate
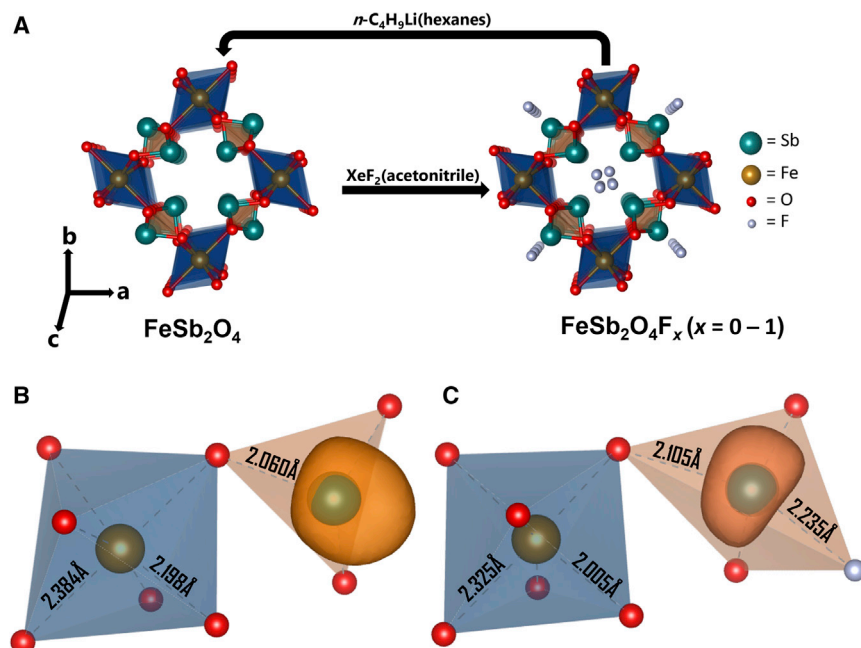
Figure 1. Reversible topochemical fluoride-ion insertion in $FeSb_2O_4$

(A) The depicted structures were obtained from previously reported Rietveld refinements.[20] Chains of edge-sharing FeO_6 octahedra are connected by corner-sharing SbO_3 trigonal pyramids.

(B and C) Magnified views of local structure as inferred from Rietveld refinements of powder XRD data (Figure S1) for (B) $FeSb_2O_4$ and (C) $FeSb_2O_4F_x$ (Tables S1 and S2 list bond lengths); Sb $5s^2$ lone pair lobes obtained from electron localization function (ELF) calculations are delineated, illustrating the distortion induced by F-ion (fluoride-ion) insertion.

that the interaction of $5s^2$ lone pairs on Sb^{3+} with the inserted fluoride ions is critical for mediating the strength of Fe-F interactions and plays a pivotal role in the reversibility of fluoride-ion insertion and the room-temperature bulk of fluoride ions across micron-sized particles.

RESULTS AND DISCUSSION

Structural transformations induced by reversible fluoride-ion insertion in $FeSb_2O_4$

$FeSb_2O_4$ was synthesized hydrothermally as reported in our previous work (see Materials & Methods in the Supporting Information therein).[20] $FeSb_2O_4$ crystallizes in the tetragonal $P4_2mbc$ space group and comprises edge-sharing FeO_6 octahedra bonded to corner-sharing Sb-centered tetrahedra; the Sb atom is bonded to three oxygen atoms and has one vertex occupied by the Sb $5s^2$ electron lone pair (thus defining a trigonal pyramidal local coordination environment). The presence of the electron lone pair at Sb opens a large, rigid, one-dimensional channel along the [001] direction of the crystal structure (Figure 1A). Topochemical fluoride-ion insertion of the hydrothermally synthesized $FeSb_2O_4$ particles was performed at 23°C with XeF_2 in acetonitrile, as reported previously.[20] Rietveld refinement of powder X-ray diffraction (XRD) data reported previously for the sample fluoridated at room temperature corresponds to a nominal stoichiometry of $x \sim 1$ in $FeSb_2O_4F_x$. Figures 1B and 1C depict the local structure of the FeO_6 octahedron and SbO_3 pseudo-tetrahedron before and after fluoride-ion insertion (Figure S1 shows the powder XRD patterns of $FeSb_2O_4$, $FeSb_2O_4F_x$, and $FeSb_2O_4F_x$ after treatment with n-butyllithium).[20] Deinsertion of fluoride ions by treatment with a strong reducing agent, n-BuLi, in hexanes at 23°C entirely restores the pristine $FeSb_2O_4$
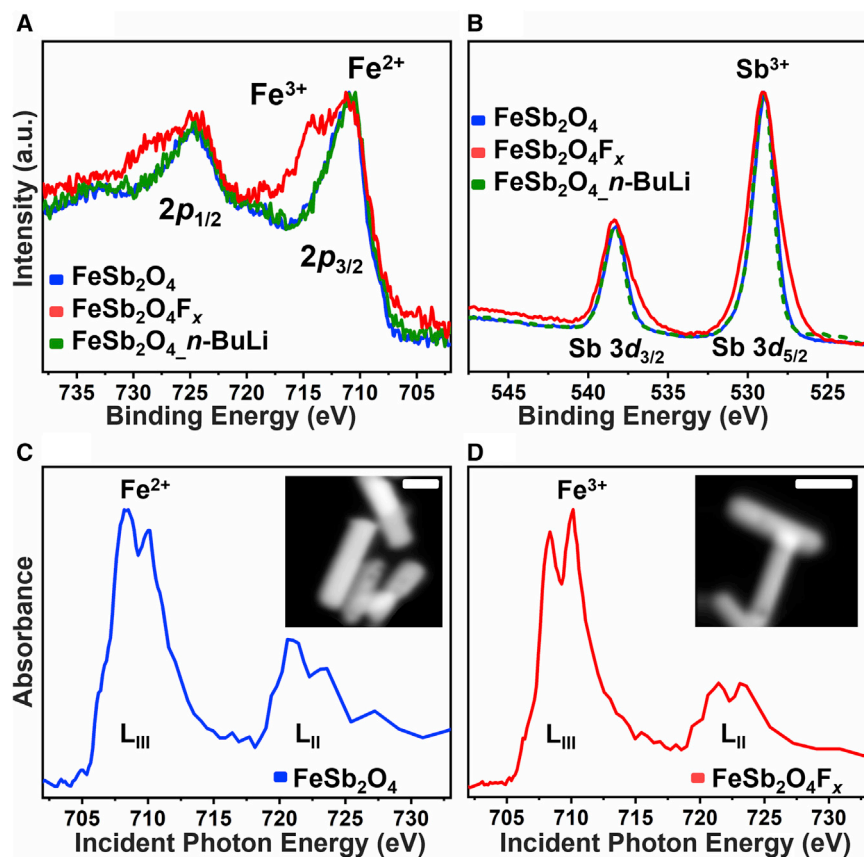
Figure 2. Evidencing oxidative fluoride-ion insertion

(A and B) High-resolution HAXPES plots at an incident energy of 5 keV for (A) Fe $2p$ and (B) Sb $3d$ core excitations collected for $FeSb_2O_4$, $FeSb_2O_4F_x$ ($x \approx 1$), and $FeSb_2O_4$ recovered after treatment of $FeSb_2O_4F_x$ with n-butyllithium.

(C) Fe $L_{III,II}$ edge XANES spectrum obtained for $FeSb_2O_4$ rods by integrating across the entire region shown in the inset STXM image (scale bar,500 nm).

(D) Fe $L_{III,II}$ edge XANES spectrum obtained for $FeSb_2O_4F_x$ ($x \approx 1$) rods by integrating across the entire region shown in the inset STXM image (scale bar, 500 nm).

structure.[20] The FeO_6 octahedra are observed to be contracted upon fluoride-ion insertion; the Fe-$O_{eq.}$ (equatorial) and Fe-$O_{ax.}$ (axial) bond lengths are decreased from 2.384 Å and 2.198 Å in $FeSb_2O_4$ to 2.325 Å and 2.005 Å in $FeSb_2O_4F_x$. The contraction of the Fe-O bond lengths suggests oxidation of iron centers. The magnitude of change in the Fe-O bond lengths in going from $FeSb_2O_4$ to $FeSb_2O_4F_x$ is characteristic of the differential in bond length between octahedrally coordinated Fe^{2+} and Fe^{3+} ions bonded to oxygen in a broad range of inorganic solids.[26] The contraction of Fe-O bonds is directly evidenced in Fe K-edge (extended X-ray absorption fine structure) EXAFS measurements, which, from X-ray absorption and emission spectroscopy measurements, is directly traceable to oxidation of iron centers (*vide infra*).[20]

Mapping changes in oxidation states upon reversible fluoride-ion insertion

As a first evaluation of electronic structure changes accompanying fluoride-ion insertion, the formal oxidation states of Fe and Sb in $FeSb_2O_4$, $FeSb_2O_4F_x$, and $FeSb_2O_4\_n$-BuLi were evaluated using HAXPES. Use of high incident photon energy beams in HAXPES enables examination of bulk (and not just surface) electronic structure.[25,27] Figure 2A plots the HAXPES data collected for Fe $2p_{3/2}$ and $2p_{1/2}$ core levels.

Emergence of features at 713 eV in the HAXPES spectra for $FeSb_2O_4F_x$ evidences oxidation of divalent iron to trivalent iron upon fluoride ion insertion (Figure 2A). Deinsertion of fluoride ions by treatment with *n*-BuLi restores the formal valence of the iron centers to their original divalent state. Further evidence of oxidative insertion of fluoride ions comes from high-resolution STXM data acquired at the Fe L_{III} and L_{II} edges (Figures 2C and 2D). To first order, L_{III}/L_{II} intensities at transition metal absorption edges are in a 2:1 ratio, which reflects their state degeneracies $(2J+1)$.[28] The more intense L_{III} edge is used widely to assign oxidation states of Fe-containing compounds.[29] The increased intensity of the Fe^{3+} L_{III} edge feature at 710 eV compared with the Fe^{2+} feature at 708 eV for $FeSb_2O_4F_x$ evidences oxidation of iron centers upon fluoride-ion insertion.[29] The Fe L_{II} edge has two features centered at 721 and 724 eV. Upon fluoridation, an inversion of the intensity ratio is observed at the Fe L_{II} edge as for the Fe L_{III} edge. However, the Fe L_{II} edge intensities are a less reliable measure of the formal oxidation state as a result of Lorentzian energy broadening of the spectral features arising from a Fe $2p$ Coster-Kronig Auger decay process.[30] Because these integrated spectra were acquired in transmission mode for the particles shown in the insets of Figures 2C and 2D, the oxidation states are representative of the entire particle volume under investigation.

The HAXPES features for the Sb $3d_{5/2}$ and $3d_{3/2}$ core levels shown in Figure 2B correspond to a formal +3 oxidation state for Sb centers in $FeSb_2O_4$. Notably, these features are broadened in the spectrum measured for $FeSb_2O_4F_x$ in comparison with $FeSb_2O_4$. With insertion of fluoride ions, the Sb coordination environment is substantially perturbed in going from SbO_3 to SbO_3F; the higher electronegativity of fluorine induces asymmetry in the electron density distribution at the Sb center, as depicted by the electron localization function (ELF) maps in Figures 1C and 1D (which is discussed in more detail below with reference to first-principles calculations). The varying extent to which the lone pair electron density is distorted for the four Sb atoms around the 1D tunnel manifests as a greater energy dispersion of the Sb-derived states, which leads to broader Sb $3d_{5/2}$ and $3d_{3/2}$ HAXPES features. The Sb states at higher binding energies correspond to the states originating from the Sb-F interaction, whereas the states at lower binding energies derive from Sb-O interactions. Notably, deinsertion of fluoride ions by *n*-BuLi treatment entirely restores the Sb $3d$ spectrum, corroborating restoration of the $FeSb_2O_4$ electronic structure. The F $1s$ core HAXPES spectrum measured for $FeSb_2O_4Fx$ is shown in Figure S2 and is consistent with the designation of the inserted species as fluoride ions.[27]

Imaging fluoride-ion diffusion in $FeSb_2O_4$ particles with high-resolution X-ray ptychography

High-resolution X-ray ptychography was performed on $FeSb_2O_4$ particles with low and high concentrations of inserted fluoride ions to image the fluoride-ion diffusion behavior by mapping the oxidation state of iron atoms.[29] X-ray ptychography is not limited by the spot size of the incident beam and can provide spatial resolution finer than the X-ray beam spot size by collecting coherent XRD patterns at various sample scan positions.[29,31] Therefore, we obtained chemical maps of iron oxidation states in $FeSb_2O_4F_x$ particles with an unprecedented spatial resolution of 6.7-nm pixel size. Figures 3A and 3B show optical density ptychography images of $FeSb_2O_4$ particles with low (nominally, $FeSb_2O_4F_{0.49}$) and high ($FeSb_2O_4F$) extent of fluoridation. The brightest domains represent the thickest regions of the particles. The oxidation state of Fe was mapped to visualize fluoride-ion diffusion. Linear fitting of the data presented in Figures 3C and 3D was performed using independently measured reference spectra corresponding to Fe^{2+} and Fe^{3+} oxidation states, as plotted in Figures
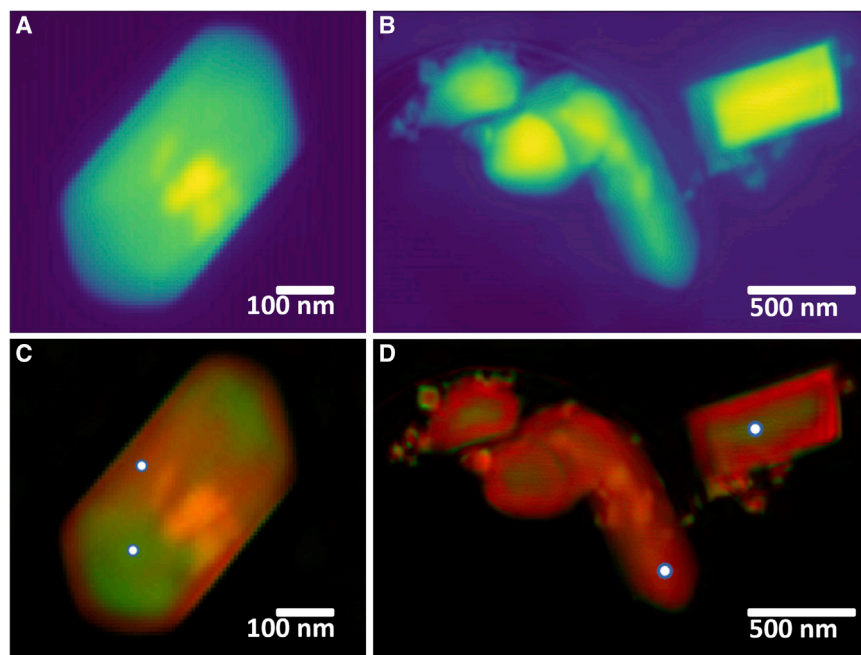
Figure 3. Imaging fluoride-ion diffusion via X-ray ptychography

(A and B) Average optical density for $FeSb_2O_4$ particles treated with a (A) low and (B) high concentration of XeF_2, measured using X-ray ptychography.

(C and D) Linear fit results for the ptychographic images obtained for the samples with (C) low fluoride-ion concentration and (D) high fluoride-ion concentrations at energy points across the Fe L_{III} edge, as shown in Figure S3, using reference spectra for Fe^{2+} and Fe^{3+} oxidation states plotted in Figure S4. Fe^{2+}, green; Fe^{3+}, red.

S3 and S4.[32] Results from the linear fit show a mixture of oxidation states for the $FeSb_2O_4F_{0.49}$ sample shown in Figure 3C tracing the contours of core-shell anion insertion. However, as the fluoride-ion concentration is increased, near-quantitative oxidation of Fe centers to a trivalent state is observed (Figure 3D). The high-resolution X-ray ptychography results show fluoride-ion insertion in the interiors of the particles, corresponding to diffusion across length scales of several hundred nanometers. The bulk diffusion of fluoride ions as observed in $FeSb_2O_4$ is in stark contrast to fluoride-ion conversion electrodes, where fluoride-ion diffusion is limited to an ~8.4-nm surface layer.[15] XRD and core-level X-ray photoemission and absorption spectroscopy measurements evidence the topochemical and oxidative nature of fluoride-ion insertion, whereas X-ray ptychography evidences bulk diffusion.

Delineating the modulation of electronic and magnetic structure of $FeSb_2O_4$ as a result of fluoride-ion insertion

To obtain a more detailed picture of the electronic structure changes in $FeSb_2O_4$ upon fluoride-ion insertion and delineate fundamental design principles related to specific anion-lattice interactions, valence band (VB) spectra of $FeSb_2O_4$ particles were acquired with and without fluoride-ion insertion using energy-variant HAXPES. The relative photoionization cross-sections of different orbitals in HAXPES decay rapidly as a function of incident photon energy but with dependences varying with the orbital angular momentum quantum number.[20–25] The photoionization cross-section of subshells with higher orbital angular momentum (e.g., d and f shells) decay relatively rapidly as a function of incident photon energy compared with s and p subshells.[33,34] Therefore, HAXPES spectra at higher incident photon energies
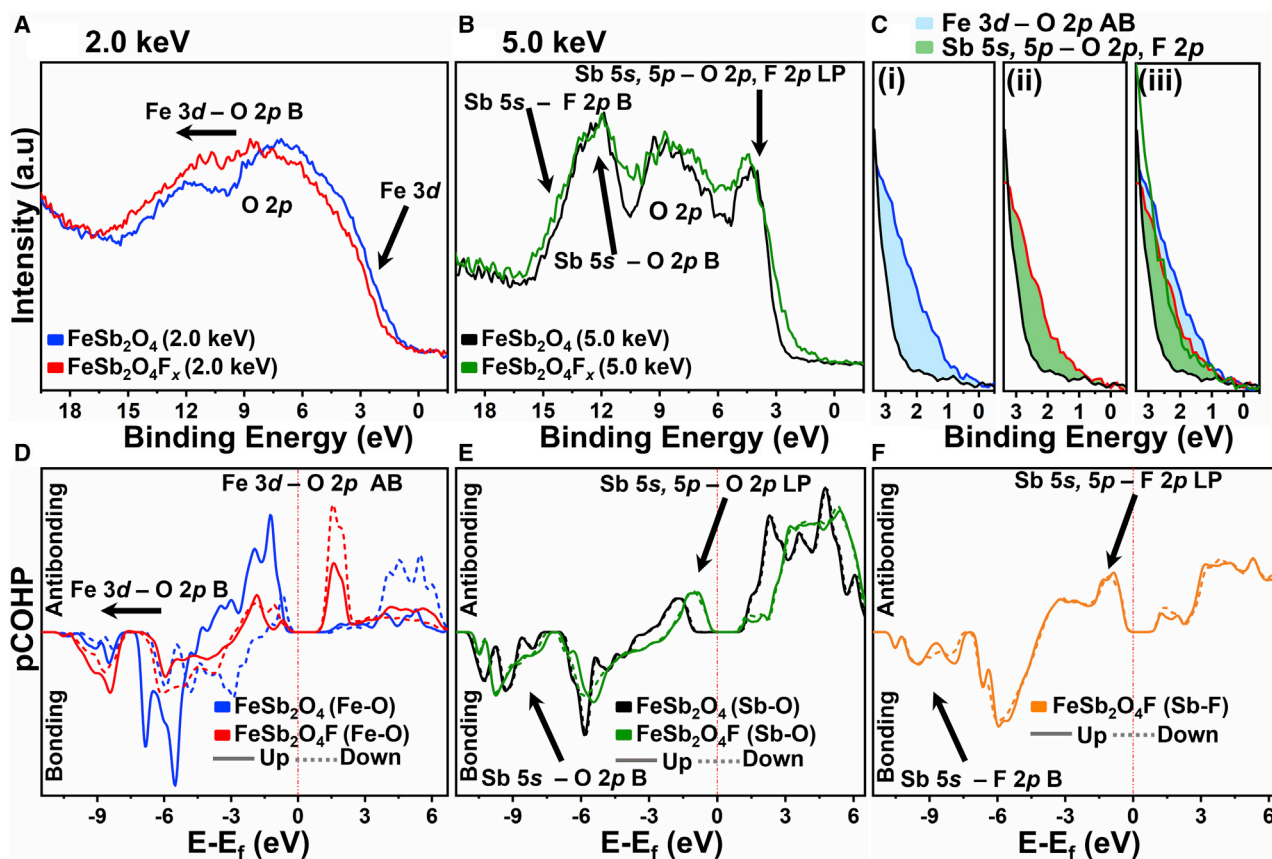
Figure 4. Evolution of the electronic structure of FeSb$_2$O$_4$ upon F-ion insertion, examined using HAXPES and crystal orbital Hamilton population (COHP) analysis

(A and B) High-resolution HAXPES data collected for FeSb$_2$O$_4$ and FeSb$_2$O$_4$F$_x$ ($x \approx 1$) at an incident photon energy of (A) 2 keV and (B) 5 keV.

(C) Overlay of the plots in (A) and (B) at the valence band maximum (VBM). (i) Comparison of HAXPES data collected for FeSb$_2$O$_4$ at 2 and 5 keV. The region highlighted in blue shows the Fe 3d – O 2p AB sates at the VBM. Because the Fe 3d – O 2p AB states have strong Fe 3d character, these states do not contribute significantly to the VB HAXPES at 5 keV. (ii) Comparison of HAXPES data collected for FeSb$_2$O$_4$F$_x$ ($x \approx 1$) at 2 and 5 keV. Upon fluoride-ion insertion in FeSb$_2$O$_4$, Sb 5s, 5p – O 2p and Sb 5s, 5p – F 2p lone pair states emerge at the VBM and are highlighted in green. (iii) Overlay of the four spectra shown in (A) and (B).

(D) COHP analysis of Fe-O interactions in FeSb$_2$O$_4$ and FeSb$_2$O$_4$F.

(E) COHP analysis for Sb-O interactions in FeSb$_2$O$_4$ and FeSb$_2$O$_4$F.

(F) COHP analysis for Sb-F interactions in FeSb$_2$O$_4$ and FeSb$_2$O$_4$F. Interactions are plotted so that B interactions between two species are negative along the y axis, whereas AB interactions are positive along the y axis. Interactions with spin-up character are plotted using a solid line, whereas interactions with spin-down character are represented as dotted lines.

(5 keV) more prominently exhibit orbital contributions from subshells with smaller angular momentum, such as stereoactive lone pair states derived from filled 5/6s orbitals of p-block cations.[21,25,33–36]

The VB of FeSb$_2$O$_4$ comprises O 2p states hybridized with Fe 3d and Sb 5s; insertion of fluoride ions further brings contributions from F 2p states in FeSb$_2$O$_4$F$_x$. To examine orbital contributions at the VB edge, VB HAXPES spectra were collected at two distinct incident photon energies, 2 and 5 keV (Figures 4A and 4B). Notable differences are observed in the VB spectra as (1) a function of incident photon energy for the same compound, enabling delineation of the orbital contributions at the VB edge, as well as for (2) pristine and fluoridated samples at the same photon energy corresponding to electronic structure changes attributable to fluoride ion insertion.

Comparing VB HAXPES spectra for $FeSb_2O_4$ and $FeSb_2O_4F_x$ at 2-keV incident photon energy reveals two key differences: (1) a notable decrease in the intensity of the states at the VB maximum (VBM) as a result of fluoridation, which provides direct evidence of oxidative insertion of fluoride ions, and (2) a blueshift of hybrid Fe 3d – O 2p states toward higher binding energies in the VB (the assignment of HAXPES features to these states is consistent with the COHP analysis in Figures 4D and 4F and atom-projected density of states in Figure S6), reflecting oxidation of iron centers. Specifically, the COHP analysis of Fe-O interactions in Figure 3D demonstrates that F-ion insertion greatly reduces Fe 3d – O 2p anti-bonding interactions at the top of the VB and introduces new anti-bonding interactions at the bottom of the conduction band. In contrast, the VB HAXPES spectra collected at 5 keV for $FeSb_2O_4$ and $FeSb_2O_4F_x$ with enhanced contribution from s- and p-derived states exhibit the opposite trend. An increase in the occupied electronic states can be observed at the top of the VB for $FeSb_2O_4F_x$ compared with $FeSb_2O_4$ (Figure 4B). Based on the COHP analysis in Figure 3E, the Sb-O anti-bonding interactions are shifted toward the VBM (shifted higher in energy) upon fluoride-ion insertion, and their intensity increases because of the weakened Sb-O bond. Destabilization of the Sb-O bond is a consequence of the emergence of Sb-F interactions. Sb-F anti-bonding interactions can also be observed at the VBM (Figure 3F), comparable with the Sb-O anti-bonding interactions. As a result of the contribution of the Sb $5s^2$ lone pair, these changes are particularly notable in HAXPES spectra acquired at 5 keV excitation energy.

To decipher the spectral changes observed upon fluoride-ion insertion at different incident photon energies in terms of specific orbital contributions, first-principles GGA+U calculations were performed, relaxing the structures deduced from Rietveld refinements.[20] Figures S5 and S6 show a direct comparison of the total and atom-projected density of states for $FeSb_2O_4$ and $FeSb_2O_4F_x$. COHP analysis for Fe-O, Sb-O, and Sb-F interactions are plotted in Figures 4D–4F for direct comparison with VB HAXPES spectra. In $FeSb_2O_4$, the states at the VBM comprise O 2p states hybridized with Fe 3d states. Filled lone-pair-derived states resulting from hybridization of O 2p with Sb 5s and 5p (specifically, the anti-bonding component of the interaction according to the revised lone pair model)[21,25,37] lie slightly deeper in the VB compared with the Fe 3d – O 2p states. It is evident from Figures 4D and S6A that (formally divalent) Fe centers are in a high-spin $(3d\uparrow)^5(3d\downarrow)^1$ configuration.[38,39] Fe 3d – O 2p bonding (B) states for spin-up Fe 3d are deep in the VB, whereas their unoccupied anti-bonding (AB) counterparts reside in the conduction band. Although the B states for spin-down Fe 3d states bonded to O 2p are deep in the VB, the occupied spin-down Fe 3d – O 2p AB states are observed at the VBM. As a result of the AB nature of this state, it has predominant orbital contributions from Fe 3d states (more electropositive Fe 3d makes the dominant contribution to the AB states, whereas the B state has a greater amount of O 2p character).

Changes in the electronic structure of $FeSb_2O_4$ as a result of fluoride-ion insertion can be deciphered by comparing the COHP analyses in Figure 4D with the HAPXES data in Figure 4A.[40,41] The loss of states at the VBM upon fluoride-ion insertion in the 2 keV HAXPES data can be directly ascribed to the loss of filled AB Fe 3d – O 2p states at the VBM that are predominantly Fe 3d spin down in origin, as shown in the calculated density of states in Figure S6A. The presence of Fe states at the VBM explains why Fe is preferentially oxidized compared with Sb centers in the $FeSb_2O_4$ lattice. In $FeSb_2O_4$ high spin, d^6 Fe centers experience a weak Jahn-Teller distortion, which is manifested in the relative elongation of the Fe-O_{axial} bonds
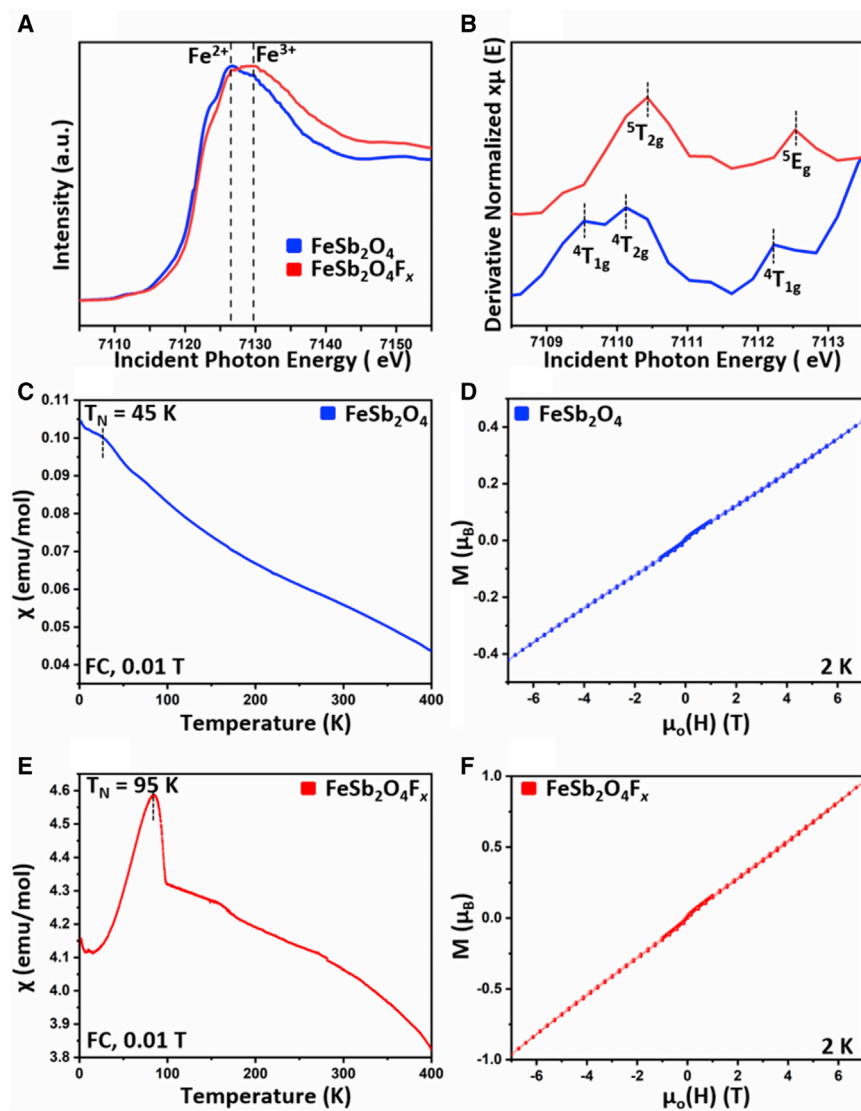
Figure 5. Probing modulation of Fe electronic structure upon fluoridation

(A) Fe K edge XANES spectra for $FeSb_2O_4$ and $FeSb_2O_4F_x$.

(B) First derivative of the pre-edge region Fe K edge XANES spectra shown in (A).

(C) Temperature dependence of the magnetic susceptibility of $FeSb_2O_4$ under an applied field of 0.01 T.

(D) Magnetization versus magnetic field curve plotted for $FeSb_2O_4$ at a temperature of 2 K.

(E) Temperature dependence of the magnetic susceptibility for $FeSb_2O_4F_x$ under an applied field of 0.01 T.

(F) Magnetization versus magnetic field curve plotted for $FeSb_2O_4F_x$ at a temperature of 2 K.

illustrated in Figure 1C.[20] The loss of electron density from the Fe 3d↓ AB states at the VBM stabilizes Fe d^5 centers, removes the Jahn-Teller distortion, and increases the overall bond order, which is reflected in stabilization of the Fe $3d$ – O $2p$ B states shown in Figure 4A (as also predicted by COHP and DFT calculations in Figures 4D and S6A), resulting in contraction of the FeO_6 octahedra, as observed in structural characterization. This $d^6 \rightarrow d^5$ shift at Fe centers was investigated further by Fe K edge XANES and magnetic susceptibility measurements (as discussed below and shown in Figure 5).

The role of Sb $5s^2$ electron lone pairs in mediating reversible fluoride-ion insertion

The photoemission spectra collected at an incident photon energy of 5 keV spotlight electronic states with s or p orbital character (and have minimal contributions from Fe $3d$ states that are dominant in the 2 keV HAXPES spectra).[25,37] Therefore, the changes in HAXPES spectra shown in Figure 4B directly probe modification of hybrid Sb $5s$, $5p$ – O $2p$ states upon fluoride-ion insertion. Three distinct features can be observed in the VB HAXPES spectra shown in Figure 4B. Sb is present in a trigonal pyramidal geometry in pristine $FeSb_2O_4$ with 3 bond pairs and one electron lone pair. The energy positioning of Sb-derived lone pair states is explicable based on the revised lone pair model.[21] The Sb $5s^2$ electron lone pairs hybridize with the empty Sb $5p$ states through O $2p$ states to form hybrid lone pair states close to the VBM. In the COHP analysis for Sb-O interactions in $FeSb_2O_4$ as plotted in Figure 4E, the Sb $5s$ – O $2p$ B states are observed deep in the VB (at ~11 eV) and have dominant Sb $5s$ character, whereas the Sb $5s$, $5p$ – O $2p$ AB states are positioned at the top of the VB (at ~2.5 eV), just below the Fe $3d$ – O $2p$ AB states.

Upon fluoride-ion insertion, the lone-pair-derived B and AB states are further hybridized with F $2p$ lone pair states near the VBM. As a result of the relatively greater electronegativity of fluorine compared with oxygen, F $2p$ states are lower in energy compared with O $2p$ and are thus better matched for hybridization with filled Sb $5s$ states. As a result, the lone-pair-derived B states are slightly stabilized, whereas the AB states are destabilized. The emergence of Sb $5s$, $5p$ – F $2p$ lone pair interactions at the VBM is shown in the COHP analysis for Sb-F interactions in Figure 4F, the F $2p$ projected density of states for $FeSb_2O_4F_x$ plotted in Figure S6C, and in the 5 keV VB HAXPES data shown in Figures 4B and 4C. Upon fluoride-ion insertion, the Fe $3d$ – O $2p$ states at the VBM in $FeSb_2O_4$ are replaced by hybrid Sb $5s$, $5p$, O $2p$, F $2p$ states in $FeSb_2O_4F_x$, reflecting oxidation of Fe. The electron lone pairs on fluoride ions further back-donate some electron density to the Sb, which fills AB Sb $5s$, $5p$ – O $2p$ lone pair states originally at the CBM; these newly occupied Sb $5s$, $5p$ – O $2p$ lone pair states can be observed in the COHP analysis for Sb-O interactions in $FeSb_2O_4F_x$ in Figure 4F, where they are present alongside the Sb $5s$, $5p$ – F $2p$ lone pair states at the VBM (Figures 4E and 4F). Notably, the shift of Sb $5s$, $5p$ – O $2p$ AB states from the CBM to VBM is also observed experimentally in Sb M_{IV} edge and O K edge XANES spectra, where the intensity of transitions to unfilled Sb states in the conduction band is attenuated upon fluoride-ion insertion in $FeSb_2O_4$ (Figure S7). Because the Sb $5s$, $5p$ – O $2p$ lone pair states at the VBM have a strong AB character, addition of electron density decreases the Sb-O bond order, which is manifested as elongation of Sb-O bonds upon fluoride-ion insertion (Figure 1C). To summarize the HAXPES and COHP data, fluoride-ion insertion results in loss of Fe $3d$ – O $2p$ AB states and emergence of Sb $5s$, $5p$ – O $2p$ and Sb $5s$, $5p$ – F $2p$ lone pair states at the VBM. Therefore, iron redox and contraction of the FeO_6 octahedron is accompanied by population of Sb-O/F AB states and expansion of SbO_3F tetrahedra.

Figure 5A plots Fe K edge XANES spectra for $FeSb_2O_4$ and $FeSb_2O_4F_x$. The dipole-allowed Fe $1s \rightarrow$ Fe $4p$ electronic transitions are most intense at 7126.4 and 7129.4 eV for $FeSb_2O_4$ and $FeSb_2O_4F_x$, respectively. These features corroborate oxidation of formally divalent iron to trivalent iron upon F-ion insertion.[38,39] A weak dipole-disallowed Fe $1s \rightarrow$ Fe $3d$ transition is observed in the pre-edge region from 7,110—7,114 eV and arises from deviations from a perfectly centrosymmetric environment.[38,39] The first derivative of the Fe K edge XANES spectra in the pre-edge region is plotted in Figure 5B.
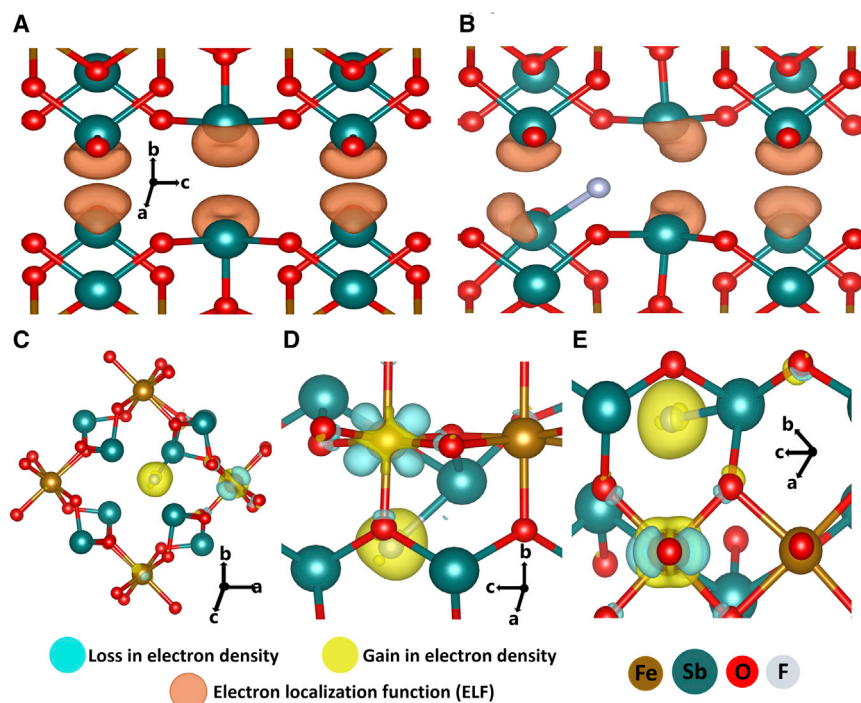
Figure 6. Mapping charge distribution upon fluoride-ion insertion

Shown are charge density difference (CDD) and ELF maps of $FeSb_2O_4$ and $FeSb_2O_4F_x$.

(A) ELF map of a $1 \times 1 \times 2$ supercell of $FeSb_2O_4$.

(B) ELF map of a $1 \times 1 \times 2$ supercell of $FeSb_2O_4$ with one fluoride ion inserted.

(C) CDD of a $1 \times 1 \times 2$ supercell of $FeSb_2O_4$ with one fluoride ion inserted.

(D) Charge redistribution around the oxidized Fe atom.

(E) Top view of the FeO_6 octahedron shown in (B).

The fine structure is attributable to the ligand field splitting of Fe $3d$ orbitals.[38,39] The three pre-edge features observed for $FeSb_2O_4$ are characteristic of high-spin ferrous compounds, corresponding to transitions from the $^5T_2$ (d6, $t_2{}^2e^2$) ground state to $^4T_1(d^{6+1}, t^1{}_2e^2)$, $^4T_1$, $^4T_2(d^{6+1}, t^2{}_2e^1)$ excited states. In contrast, upon F-ion insertion, the two observed features are attributable to transitions from the $^6A_1(t_2{}^3e^2)$ ground state to $^5T_2(t_2{}^2e^2)$ and $^5E(t_2{}^3e^1)$ excited states characteristic of high-spin ferric compounds.[38,39] Magnetic susceptibility measurements further support the high-spin $d^6 \rightarrow$ high-spin d^5 change in iron electron configuration upon fluoridation. Figures 5C and 5E show the magnetic susceptibilities as a function of temperature for $FeSb_2O_4$ and $FeSb_2O_4F_x$, respectively, and show that F-ion insertion and concomitant Fe^{2+} oxidation bring about a significant change in magnetic behavior. $FeSb_2O_4$ and $FeSb_2O_4F_x$ exhibit antiferromagnetic behavior but with Neel transition temperatures (T_N) of 45 K and 95 K, respectively. The increased T_N upon F-ion insertion indicates strengthening of intra- and interchain magnetic exchange interactions, which is concordant with the contraction of FeO_6 octahedra and the accompanying distortion of the 1D tunnel. In addition, $FeSb_2O_4F_x$ shows a decrease in susceptibility below T_N and a relatively broad maximum around the T_N features, which are not observed in $FeSb_2O_4$, derived likely in part from a diverse range of local magnetic ordering arising from F-ion disorder across tunnel interstitial sites. The field dependence of magnetization of $FeSb_2O_4$ and $FeSb_2O_4F_x$ were measured at 2 K, as shown in Figures 5D and 5F, respectively. The plot shows an increase in saturation magnetization value from 0.4 to 1.0 μ_B after fluoridation, further indicative of change from high-spin Jahn-Teller distorted $d^6 \rightarrow$ high-spin undistorted d^5 upon F-ion insertion.[42–44]

To visualize the changes in electronic and atomistic structure upon fluoride-ion insertion, ELF, and charge density difference (CDD) plots were calculated for $FeSb_2O_4$ and $FeSb_2O_4F_x$. The ELFs for $FeSb_2O_4$ and $FeSb_2O_4$ with addition of a fluoride ion are plotted in Figures 6A and 6B, respectively. In $FeSb_2O_4$, the lone pair electrons are repelled by Sb-O B electron pairs and are protuberant within the tunnels (Figure 6A). Upon introduction of a fluoride ion, the lone pair on the Sb atom coordinating with the fluoride-ion experiences repulsion from four B pairs (3Sb-O and Sb-F), strongly distorting Sb 5s-derived lone pairs in the vicinity of the fluoride ion (Figure 6B).

CDDs upon fluoride ion insertion are plotted in Figures 6C–6E to visualize the electron density change according to

$$\Delta\rho(r) = \rho FeSb_2O_4F_{0.125}(r) - \rho FeSb_2O_4(r) - \rho F(r), \qquad \text{(Equation 1)}$$

where $\rho FeSb_2O_4F_{0.125}(r)$ represents the charge density for a $1 \times 1 \times 2$ $FeSb_2O_4$ superlattice inserted with one fluoride ion, $\rho F(r)$ is the electron density of an isolated F atom at the same coordinates as the fluoride ion in $FeSb_2O_4F_{0.125}$, and $\rho FeSb_2O_4(r)$ is the charge density obtained for a $FeSb_2O_4$ unit cell without fluoride-ion insertion. Figure 6C shows stabilization of a fluoride ion inserted in $FeSb_2O_4$ in a tetrahedral interstitial site surrounded by four Sb atoms. Concordant with the ELF map in Figure 6B, four Sb atoms are associated with the inserted fluoride ion; however, preferential coordination is observed to one Sb atom, resulting in slight off-centering of the fluoride ion from the tetrahedral site. A modest charge redistribution at the Sb atom in Figures 6D and 6E further reflects a distortion of the $5s^2$ lone pair as a result of the additional repulsions from the Sb-F bond and F 2p lone pairs (and is the origin of the broadening of Sb HAXPES spectra observed upon fluoridation in Figure 2B).

The Sb atom coordinated to the fluoride ion and the Fe atom undergoing oxidation is bridged through an oxygen atom. Redistribution of electron density is observed around the Fe center. Figures 6D and 6E depict lateral and top views of changes in electron density around the Fe atom, illustrating a gain of electron density along with the Fe-O bonds, consistent with the shortening of bond length observed in real-space XRD and EXAFS measurements, and loss of electron density from Fe 3d states, as observed in HAXPES and Fe L_{III} edge XANES measurements. To quantify changes in electron density with fluoride-ion insertion, Bader charge analysis was also performed. Figure 7A shows an increase from +1.39 to +1.79 for an iron atom as a result of fluoride-ion insertion; a more modest redistribution of charge is evidenced for the Sb atom upon fluoride-ion insertion (Figure 7B). The results corroborate the redox events at the iron site and delineate the role of distortion of Sb stereoactive lone pairs in accommodating fluoride ions within the tunnel. Table S3 lists the average and range of charge density of Bader charges (Figure S8).

Figure 7C provides a molecular orbital diagram representation to summarize the electronic structure modulations in $FeSb_2O_4$ as mapped through HAXPES, XANES, COHP, and electronic structure calculations. States with predominantly Fe 3d character (AB Fe 3d – O 2p states) are the highest occupied states in $FeSb_2O_4$ and are positioned higher in energy compared with Sb-O lone-pair states. Fluoride ion insertion brings about oxidation of iron and loss of electron density from Fe 3d – O 2p AB states, strengthening Fe-O bonds and resulting in contraction of FeO_6 octahedra, as surmised from powder XRD and EXAFS data. Concurrently, Sb-F lone pair states emerge at the VBM alongside AB Sb-O lone pair states that were originally situated within the conduction band manifold and are filled as a result of back-donation of
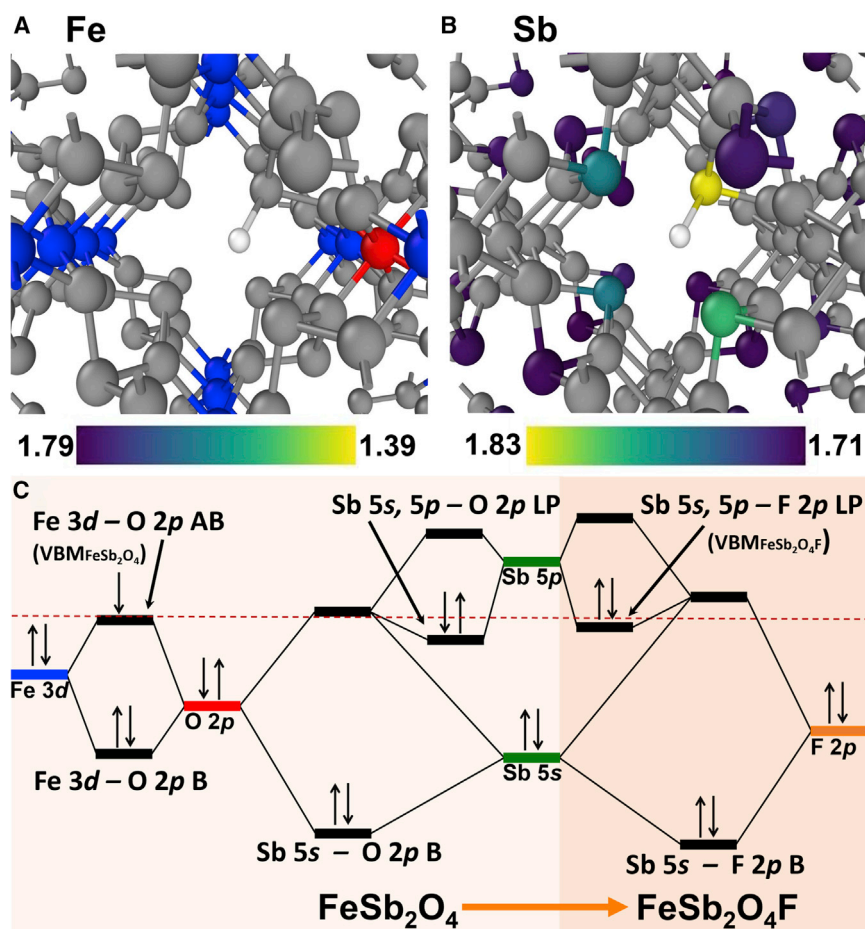
Figure 7. A molecular orbital perspective of electronic structure modulation of $FeSb_2O_4$ with fluoridation

(A) The net charge on Fe atoms in $FeSb_2O_4F_x$, calculated via Bader charge analysis (F, white; Sb and O, gray; Fe, charge scale).

(B) The net charge on Sb atoms in $FeSb_2O_4F_x$, calculated via Bader charge analysis (F, white; Fe and O, gray; Sb, charge scale).

(C) Molecular orbital diagram showing the relative position of Sb 5s, 5p – O 2p, and Sb 5s, 5p – F 2p lone pair states relative to the Fe 3d – O 2p AB states.

electron density from fluoride ions. SbO_3LP tetrahedra are transformed through weakening of Sb-O interactions (concomitant with stronger Fe-O interactions) to a distorted SbO_3FLP square pyramid coordinating a fluoride ion. All four Sb $5s^2$ lone pairs adjacent to the inserted fluoride ion are strongly distorted (Figure 5B).[45–47] In essence, although the Sb interaction stabilizes fluoride-ion insertion within the 1D tunnel of $FeSb_2O_4$ and mediates the redox reaction at the iron center (Figures 4E, 4F S6B, and S6C), the repulsions between Sb $5s^2$ and F 2p lone pairs result in a relatively weak Sb-F bond that can be formed and broken at room temperature. Stronger Sb-F interactions (in the absence of lone pair repulsion) would imply more stable coordination sites for the inserted fluoride ions, which would be reflected in a higher migration barrier. Therefore, destabilization of Sb $5s^2$ lone pair states upon fluoride-ion insertion (Figure 7C) is pivotal for the relative ease of diffusion of fluoride ions, enabling homogeneous fluoride-ion insertion and diffusion across micron-sized dimensions. Figure 7 illustrates that Sb^{3+} lone-pair-derived states are destabilized upon fluoride ion insertion; restoring these states provides a driving force for fluoride

ion deinsertion and facilitates diffusion in a manner akin to the role of frustrated coordination proposed for the mobility of multivalent cations.[48,49]

Figure S9 shows several possible diffusion pathways through the 1D tunnel, as calculated using nudged elastic band (NEB) DFT calculations. In contrast to the propagation of reaction-diffusion fronts necessary for conversion reactions, $FeSb_2O_4$ has an abundance of interstitial sites, accessible redox centers, and the ability to accommodate the inserted ions without large lattice volume alteration (<1% for fluoride-ion insertion up to $FeSb_2O_4F$). The migration barrier for fluoride-ion diffusion in $FeSb_2O_4$ (570 meV) is substantially lower compared with La_2CoO_4 (830 meV).[18] To place these results in context, migration barriers of less than 600–750 meV are expected to enable room-temperature diffusivity for submicron-sized particles. Assuming a temperature-independent jumping frequency (v_0) of 10^{13} s^{-1} for fluorideions,[18] we calculate a diffusivity of 3.7×10^{-13} cm$^2 \cdot$s^{-1}, which suggests that, at C rates slower than 1C, room-temperature diffusion will be possible across a particle size of 0.36 μm, as indeed observed here (Figure 3).[4] Unlike La ions in La_2CoO_4, which are primarily electrostatic with a limited role in mediating fluoride-ion insertion, the trivalent Sb centers and their stereoactive electron lone pairs play a critical role in mediating fluoride-ion insertion and deinsertion. In the absence of a viable electrolyte that enables room-temperature electrochemical fluoridation, a detailed experimental evaluation of fluoride-ion diffusivity as a function of the state of charge was not possible. In analogy with Li-ion and multivalent cation migration,[4,20] in the absence of a phase transition that substantially alters the 1D tunnel structure, it is expected that fluoride-ion diffusivity will be decreased with increasing fluoridation as a greater proportion of the interstitial sites in the tunnel are occupied.

We identified fundamental design principles underpinning reversible room-temperature fluoride-ion insertion and bulk diffusion in $FeSb_2O_4$, delineating, the non-innocent role of stereoactive lone pair electrons of trivalent antimony in mediating reversibility and fluoride-ion diffusion. Powder XRD measurements illustrate the positioning of fluoride ions within the 1D tunnels of $FeSb_2O_4$, where they are ensconced between four antimony centers. High-resolution X-ray ptychography measurements illustrate bulk diffusion of fluoride ions at room temperature. HAXPES, STXM, XANES, and magnetic susceptibility measurements provide independent verification that fluoride-ion insertion brings about oxidation of Fe centers. Electron density from Fe $3d-$O $2p$ AB states at the VBM is used in the oxidative insertion reaction, bringing about a pronounced contraction of FeO_6 octahedra. Although Sb centers are not formally oxidized, Sb $5s^2$ electron lone pairs interact with F $2p$ states, yielding new states at the top of the VB. Coordination of fluoride ions to Sb sites results in distortion of electron lone pairs and brings about an overall expansion of the SbO_3FLP coordination environment. The Sb $5s^2$ electron lone pair repulsions are fundamentally responsible for relatively weak Sb-F coordination. The weak Sb-F bond in fluoridated $FeSb_2O_4$ enables fluoride ion deinsertion upon treatment with n-BuLi at room temperature and underpins the facile room-temperature diffusion of fluoride ions across micron-sized particles. Sb^{3+} lone-pair-derived states are destabilized upon fluoride-ion insertion because of the decreased Sb $5s$, $5p$ hybridization with O $2p$ states; restoring these states through thermally activated Sb-F bond scission provides a driving force for fluoride-ion deinsertion and facilitates diffusion in a manner akin to the role of frustrated coordination proposed for the mobility of multivalent cations.[46,47] Separation of the primary redox center (Fe) from the coordination site (Sb) allows distribution of the structural distortions among different structural motifs within the lattice. Therefore, $FeSb_2O_4$ can be reversibly fluoridated with complete recovery of the crystal lattice. A substantial constraint to

accomplishing electrochemical fluoride-ion insertion (instead of chemical redox examined here) is the paucity of suitable room-temperature fluoride-ion electrolytes.[11,12] Although several possibilities have been reported, such as quaternary ammonium salts dissolved in ionic liquids,[15] there remain considerable challenges with operating windows and compatibility with electrode materials and current collectors.[19] We hope that the demonstration of design principles for room-temperature insertion/deinsertion and bulk diffusion of fluoride ions will spur development of liquid and solid electrolytes compatible with this electrode. The design principles gleaned from this work pave the way for examination of a broad range of potential intercalation hosts pairing transition metal redox sites with p-block cations bearing stereoactive lone pairs to mediate anion-lattice interactions.

EXPERIMENTAL PROCEDURES

Resource availability

Lead contact

Further information and requests for resources and reagents should be directed to and will be fulfilled by the lead contact, Sarbajit Banerjee (banerjee@chem.tamu.edu).

Materials availability

The study did not generate any new unique reagents.

Data and code availability

All data related to this study included in the article and supplemental information will be provided by the lead contact, Sarbajit Banerjee (banerjee@chem.tamu.edu) upon reasonable request.

Hydrothermal synthesis of $FeSb_2O_4$

$Fesb_2O_4$ was synthesized hydrothermally as reported previously[20] by mixing stoichiometric amounts of 0.334 M $(NH_4)_2Fe(SO_4)_2 \cdot 6H_2O$ aqueous solution with a 0.667 M $SbCl_3$ aqueous solution prepared in 4 M HCl. The resulting mixture was titrated with an 8 M aqueous solution of NaOH under constant stirring to obtain a pH of 12. The solution was then transferred to a polytetrafluoroethylene-lined high-temperature autoclave (Parr) and heated in a box furnace at 210°C for 24 h. The solid product was separated from the supernatant by centrifugation and was washed twice with distilled water and once with isopropanol.

Fluoride ion insertion in $FeSb_2O_4$ at 23°C

All fluoridation and defluoridation reactions were performed in an argon-filled glovebox maintained at O_2 and H_2O levels of 0.1 ppm and 0.1 ppm, respectively. Fluoridation was carried out by stirring $FeSb_2O_4$ with a 5-fold molar excess amount of XeF_2 in acetonitrile at 23°C.[20] The excess acetonitrile was decanted, and the obtained product was washed three times with 10 mL acetonitrile. The powder was dried and stored under argon.

Defluoridation of $FeSb_2O_4F_x$

To extract fluoride ions, $FeSb_2O_4F_x$ was mixed with a molar excess of *n*-BuLi in hexanes (*n*-BuLi:$FeSb_2O_4F_x$ = 5:1) at 23°C as reported previously.[20] The supernatant was decanted, and the obtained product was washed with hexanes and centrifuged three times to remove any unreacted *n*-BuLi.

XRD and structural characterization

Powder XRD patterns were collected in Brag-Brentano geometry on a Bruker D8-focus diffractometer (Cu K-α, λ = 1.5418 Å; 40-kV voltage; 25-mA current). All

Rietveld refinements were performed using the EXPGUI user interface of GSAS.[50] All crystal structure renditions depicted in this article were prepared using the Vesta III software suite (JP-minerals).[51]

XANES

Fe K edge XANES spectra were collected at the Advanced Light Source (ALS) bending-magnet beamline 10.3.2 (2.4–17 keV). The storage ring is operated at 500 mA and 1.9 GeV. Spectra were collected in fluorescence mode by continuously scanning the Si (111) monochromator. Fe foil was used as a calibration standard. LabVIEW custom software was used to perform deadtime correction, glitch removal, energy calibration, pre-edge subtraction, and post-edge normalization. The Athena suite of programs in the IFEFFIT package was used for further processing of the data.[52]

Sb M and O K NEXAFS measurements were carried out at the National Synchrotron Light Source II of Brookhaven National Laboratory beamline SST-1 operated by the National Institute of Standards and Technology. Measurements were performed in partial electron yield (PEY) mode with a nominal resolution of 0.1 eV. The PEY signal was normalized to the incident beam intensity of a clean gold grid to eliminate the effects of any incident beam fluctuations and optics absorption features.

HAXPES

HAXPES measurements were performed at the National Institute of Standards and Technology beamline SST-2 of the National Synchrotron Light Source II of Brookhaven National Laboratory. Measurements were performed at approximately 2 keV photon energy with a pass energy of 200 eV and a step size of 0.85 eV with the analyzer axis oriented parallel with the photoelectron polarization vector. The data at 5 keV were collected with a 500-eV energy filter. The higher excitation of HAXPES circumvents deleterious charging issues that are common to ultraviolet and soft X-ray photoelectron spectroscopy.[36] Photon energy selection was accomplished using a double Si (111) crystal monochromator. No evidence of charging was observed during our measurements. The beam energy was aligned to the Fermi level of a silver foil before measurements.

STXM

STXM measurements at the Fe L edge were performed at the bending magnet beamline 5.3.2.1 and the insertion device beamline 7.0.1.2 (COSMIC) of the ALS. Powder samples were suspended in isopropanol and drop-casted on silicon nitride membrane windows for analysis. Data alignment, post-processing, and region of interest (ROI) analysis was performed using the aXis2000 software suite (http://unicorn.mcmaster.ca/aXis2000.html).

Magnetic measurements

Magnetic measurements were carried out on a Quantum Design magnetic property measurement system using the Quantum Design superconducting quantum interference device (SQUID) magnetometer option. Field cooled (FC) measurements were performed in a temperature range of 2–400 K with an applied field up to 0.01 T. Field-dependent magnetization measurements were performed at 2 K.

Ptychography

Ptychography measurements at the Fe K edge were performed at the insertion device beamline 7.0.1.2 (COSMIC) of the ALS.

Computational methods

Electronic structure calculations were performed using DFT as implemented in the Vienna *ab initio* simulation package (VASP).[53,54] Initial atomic positions for $FeSb_2O_4$ and $FeSb_2O_4F$ were obtained from the Rietveld refinement of the powder XRD data. The projected augmented wave (PAW) formalism was used to model electron-ion interactions.[55,56] A kinetic energy cutoff of 520 eV was used for plane-wave basis restriction. Electronic exchange and correlation effects were included using the generalized gradient approximation based on the Perdew-Burke-Ernzerhof functional (GGA-PBE).[57] A Hubbard correction of $U = 5.3$ eV was used to account for strong electron correlation in the Fe 3d electrons as benchmarked in a previous study.[58] A Γ-point centered Monkhorst-Pack reciprocal grid of $4 \times 4 \times 2$ points was used for relaxation of $1 \times 1 \times 2$ supercell structures. The structures were considered to be relaxed when each Cartesian force component was less than 0.01 eV/Å unless otherwise noted. Bader charge was calculated using VASP output.[59] The output from Bader charge as presented here was plotted in Ovito.[60]

Fluoride ion migration barriers were calculated by employing climbing-image nudged elastic band (NEB) calculations as implemented in VASP.[61] We used $2 \times 2 \times 2$ $FeSb_2O_4$ supercells for NEB calculations. The endpoints were relaxed until each Cartesian force component was less than 0.001 eV Å^{-1}, whereas for the forces along the NEB path, the convergence criterion was 0.02 eV Å^{-1}. Diffusivity (D) was estimated according to the following equation:[62]

$$D = \frac{l^2 v_0}{2n}\exp\left(-\frac{E_a}{kT}\right), \qquad \text{(Equation 2)}$$

where l is the jumping distance, v_0 is the temperature-independent jumping frequency, and n is the dimensionality of the material under investigation.

We also performed a spin-polarized single-point energy calculation to calculate the projected density of states (pDOS) with the software package Local Orbital Suite Toward Electronic-Structure Reconstruction (LOBSTER).[41,63] We use the Bunge's description for the local basis functions needed for the projection calculations with the 2s and 2p orbitals for oxygen and fluorine, 3d and 4s for iron, and the 5p and 5s for antimony. The absolute charge spilling is lower than 1.31% in all cases.

AUTHOR CONTRIBUTIONS

S.B. directed the research. W.Z. and S.B. conceptualized and designed the experiments. W.Z. conducted and analyzed the data from powder X-ray diffraction, STXM, HAXPES, X-ray ptychography, XANES, density of states, charge density difference, electron localization function, Bader charge analysis, and nudged elastic band experiments. G.A. conducted the magnetic measurements and analyzed the data. S.P.-B. carried out COHP calculations. J.L.A. performed Rietveld analysis of the powder X-ray diffraction data. Y.A. helped with Bader charge analysis. C.W. helped with setting up HAXPES experiments and data collection. C.J. helped with setting up XANES experiments and data collection. Y.-S.Y. and D.A.S. helped with setting up X-ray ptychography experiments, data collection, and data analysis. S.C.F. helped with setting up XANES experiments. D.A.F. helped with setting up XANES and HAXPES experiments. J.G. provided guidance regarding analysis of XANES data. D.P. provided guidance regarding first-principle calculations via DFT. W.Z., G.A., and S.B. contributed to writing the paper. All authors discussed the experimental results.

DECLARATION OF INTERESTS

The authors declare no competing interests.

REFERENCES

1. Dunn, B., Kamath, H., and Tarascon, J.-M. (2011). Electrical energy storage for the grid: a battery of choices. Science 334, 928–935.

2. Cano, Z.P., Banham, D., Ye, S., Hintennach, A., Lu, J., Fowler, M., and Chen, Z. (2018). Batteries and Fuel Cells for Emerging Electric Vehicle Markets. Nat. Energy 3, 279–289.

3. Liang, Y., Dong, H., Aurbach, D., and Yao, Y. (2020). Current Status and Future Directions of Multivalent Metal-Ion Batteries. Nat. Energy 5, 646–656.

4. Canepa, P., Sai Gautam, G., Hannah, D.C., Malik, R., Liu, M., Gallagher, K.G., Persson, K.A., and Ceder, G. (2017). Odyssey of Multivalent Cathode Materials: Open Questions and Future Challenges. Chem. Rev. 117, 4287–4341.

5. Park, M., Ryu, J., Wang, W., and Cho, J. (2016). Material Design and Engineering of Next-Generation Flow-Battery Technologies. Nat. Rev. Mater. 2, 1–18.

6. Andrews, J.L., and Banerjee, S. (2018). It's Not Over until the Big Ion Dances: Potassium Gets Its Groove On. Joule 2, 2194–2197.

7. Mohtadi, R., Tutusaus, O., Arthur, T.S., Zhao-Karger, Z., and Fichtner, M. (2021). The Metamorphosis of Rechargeable Magnesium Batteries. Joule 5, 581–617.

8. Vaalma, C., Buchholz, D., Weil, M., and Passerini, S. (2018). A Cost and Resource Analysis of Sodium-Ion Batteries. Nat. Rev. Mater. 3, 1–11.

9. Chayambuka, K., Mulder, G., Danilov, D.L., and Notten, P.H.L. (2018). Sodium-Ion Battery Materials and Electrochemical Properties Reviewed. Adv. Energy Mater. 8, 1–3.

10. Anji Reddy, M., and Fichtner, M. (2011). Batteries Based on Fluoride Shuttle. J. Mater. Chem. 21, 17059–17062.

11. Gschwind, F., Rodriguez-Garcia, G., Sandbeck, D.J.S., Gross, A., Weil, M., Fichtner, M., and Hörmann, N. (2016). Fluoride Ion Batteries: Theoretical Performance, Safety, Toxicity, and a Combinatorial Screening of New Electrodes. J. Fluor. Chem. 182, 76–90.

12. Nowroozi, M.A., Mohammad, I., Molaiyan, P., Wissel, K., Munnangi, A.R., and Clemens, O. (2021). Fluoride Ion Batteries - Past, Present, and Future. J. Mater. Chem. A Mater. Energy Sustain. 9, 5980–6012.

13. Thieu, D.T., Fawey, M.H., Bhatia, H., Diemant, T., Chakravadhanula, V.S.K., Behm, R.J., Kübel, C., and Fichtner, M. (2017). CuF2 as Reversible Cathode for Fluoride Ion Batteries. Adv. Funct. Mater. 27, 1–11.

14. Gschwind, F., and Bastien, J. (2015). Parametric Investigation of Room-Temperature Fluoride-Ion Batteries: Assessment of Electrolytes, Mg-Based Anodes, and BiF3-Cathodes. J. Mater. Chem. A Mater. Energy Sustain. 3, 5628–5634.

15. Davis, V.K., Bates, C.M., Omichi, K., Savoie, B.M., Momčilović, N., Xu, Q., Wolf, W.J., Webb, M.A., Billings, K.J., Chou, N.H., et al. (2018). Room-temperature cycling of metal fluoride electrodes: Liquid electrolytes for high-energy fluoride ion cells. Science 362, 1144–1148.

16. Nowroozi, M.A., Wissel, K., Rohrer, J., Munnangi, A.R., and Clemens, O. (2017). LaSrMnO4: Reversible Electrochemical Intercalation of Fluoride Ions in the Context of Fluoride Ion Batteries. Chem. Mater. 29, 3441–3453.

17. Nowroozi, M.A., Ivlev, S., Rohrer, J., and Clemens, O. (2018). La$_2$CoO$_4$: A New Intercalation Based Cathode Material for Fluoride Ion Batteries with Improved Cycling Stability. J. Mater. Chem. A Mater. Energy Sustain. 6, 4658–4669.

18. Hartman, S.T., and Mishra, R. (2020). Layered Electrides as Fluoride Intercalation Anodes. J. Mater. Chem. A Mater. Energy Sustain. 8, 24469–24476.

19. Bashian, N.H., Zuba, M., Irshad, A., Becwar, S.M., Vinckeviciute, J., Rahim, W., Griffith, K.J., McClure, E.T., Papp, J.K., McCloskey, B.D., et al. (2021). Electrochemical Oxidative Fluorination of an Oxide Perovskite. Chem. Mater. 33, 5757–5768.

20. Zaheer, W., Andrews, J.L., Parija, A., Hyler, F.P., Jaye, C., Weiland, C., Yu, Y.S., Shapiro, D.A., Fischer, D.A., Guo, J., et al. (2020). Reversible Room-Temperature Fluoride-Ion Insertion in a Tunnel-Structured Transition Metal Oxide Host. ACS Energy Lett. 5, 2520–2526.

21. Walsh, A., Payne, D.J., Egdell, R.G., and Watson, G.W. (2011). Stereochemistry of post-transition metal oxides: revision of the classical lone pair model. Chem. Soc. Rev. 40, 4455–4463.

22. Waghmare, U.V., Spaldin, N.A., Kandpal, H.C., and Seshadri, R. (2003). First-Principles Indicators of Metallicity and Cation off-Centricity in the IV-VI Rocksalt Chalcogenides of Divalent Ge, Sn, and Pb. Phys. Rev. B 67, 125111.

23. Fabini, D.H., Laurita, G., Bechtel, J.S., Stoumpos, C.C., Evans, H.A., Kontos, A.G., Raptis, Y.S., Falaras, P., Van der Ven, A., Kanatzidis, M.G., and Seshadri, R. (2016). Dynamic Stereochemical Activity of the Sn$^{(2+)}$ Lone Pair in Perovskite CsSnBr$_3$. J. Am. Chem. Soc. 138, 11820–11832.

24. Cho, J., Sheng, A., Suwandaratne, N., Wangoh, L., Andrews, J.L., Zhang, P., Piper, L.F.J., Watson, D.F., and Banerjee, S. (2019). The Middle Road Less Taken: Electronic-Structure-Inspired Design of Hybrid Photocatalytic Platforms for Solar Fuel Generation. Acc. Chem. Res. 52, 645–655.

25. Dang, U., Zaheer, W., Zhou, W., Kandel, A., Orr, M., Schwenz, R.W., Laurita, G., Banerjee, S., and MacAluso, R.T. (2020). Lattice Anharmonicity of Stereochemically Active Lone Pairs Controls Thermochromic Band Gap Reduction of PbVO$_3$Cl. Chem. Mater. 32, 7404–7412.

26. Gagné, O.C., and Hawthorne, F.C. (2020). Bond-length distributions for ions bonded to oxygen: results for the transition metals and quantification of the factors underlying bond-length variation in inorganic solids. IUCrJ 7, 581–629.

27. Naumkin, A.V., Kraut-Vass, A., Gaarenstroom, S.W., and Powell, C.J. (2012). NIST X-ray Photoelectron Spectroscopy Database. https://srdata.nist.gov/xps/.

28. De Groot, F.M.F. (2009). AWARD PAPER: XANES Spectra of Transition Metal Compounds. J. Phys. Conf. Ser. 190, 1–9.

29. Lim, J., Li, Y., Alsem, D.H., So, H., Lee, S.C., Bai, P., Cogswell, D.A., Liu, X., Jin, N., Yu, Y.S., et al. (2016). Origin and hysteresis of lithium compositional spatiodynamics within battery primary particles. Science 353, 566–571.

30. Baker, M.L., Mara, M.W., Yan, J.J., Hodgson, K.O., Hedman, B., and Solomon, E.I. (2017). K- and L-edge X-ray Absorption Spectroscopy (XAS) and Resonant Inelastic X-ray Scattering (RIXS) Determination of Differential Orbital Covalency (DOC) of Transition Metal Sites. Coord. Chem. Rev. 345, 182–208.

31. Shapiro, D.A., Babin, S., Celestre, R.S., Chao, W., Conley, R.P., Denes, P., Enders, B., Enfedaque, P., James, S., Joseph, J.M., et al. (2020). An ultrahigh-resolution soft x-ray microscope for quantitative analysis of chemically heterogeneous nanomaterials. Sci. Adv. 6, 1–8.

32. Farmand, M., Celestre, R., Denes, P., Kilcoyne, A.L.D., Marchesini, S., Padmore, H., Tyliszczak, T., Warwick, T., Shi, X., Lee, J., et al. (2017). Near-Edge X-Ray Refraction Fine Structure Microscopy. Appl. Phys. Lett. 110, 1–5.

33. Regoutz, A., Mascheck, M., Wiell, T., Eriksson, S.K., Liljenberg, C., Tetzner, K., Williamson, B.A.D., Scanlon, D.O., and Palmgren, P. (2018). A novel laboratory-based hard X-ray photoelectron spectroscopy system. Rev. Sci. Instrum. 89, 073105.

34. Kalha, C., Fernando, N.K., Bhatt, P., Johansson, F.O.L., Lindblad, A., Rensmo, H., Medina, L.Z., Lindblad, R., Siol, S., Jeurgens, L.P.H., et al. (2021). Hard x-ray photoelectron spectroscopy: a snapshot of the state-of-the-art in 2020. J. Phys. Condens. Matter 33, 1–44.

35. Yeh, J.J., and Lindau, I. (1985). Atomic and Nuclear Data Tables. 32, 1–155.

36. Weiland, C., Rumaiz, A.K., Pianetta, P., and Woicik, J.C. (2016). Recent Applications of Hard X-Ray Photoelectron Spectroscopy. J. Vac. Sci. Technol. A 34, 030801.

37. Razek, S.A., Popeil, M.R., Wangoh, L., Rana, J., Suwandaratne, N., Andrews, J.L., Watson, D.F., Banerjee, S., and Piper, L.F.J. (2020). Designing Catalysts for Water Splitting Based on Electronic Structure Considerations. Electron. Struct. 2, 1–22.

38. Haas, O., Deb, A., Cairns, E.J., and Wokaun, A. (2005). Synchrotron X-Ray Absorption Study of LiFePO$_4$ Electrodes. J. Electrochem. Soc. 152, A191–A196.

39. Westre, T.E., Kennepohl, P., DeWitt, J.G., Hedman, B., Hodgson, K.O., and Solomon, E.I. (1997). A Multiplet Analysis of Fe K-Edge 1s → 3d Pre-Edge Features of Iron Complexes. J. Am. Chem. Soc. 119, 6297–6314.

40. Dronskowski, R., and Blochl, P.E. (1993). Crystal orbital Hamilton populations (COHP): energy-resolved visualization of chemical bonding in solids based on density-functional calculations. J. Phys. Chem. 97, 8617–8624.

41. Nelson, R., Ertural, C., George, J., Deringer, V.L., Hautier, G., and Dronskowski, R. (2020). LOBSTER: Local orbital projections, atomic charges, and chemical-bonding analysis from projector-augmented-wave-based density-functional theory. J. Comput. Chem. 41, 1931–1940.

42. Gonzalo, J.A., Cox, D.E., and Shirane, G. (1966). The Magnetic Structure of FeSb$_2$O$_4$. Phys. Rev. 147, 415–418.

43. Whitaker, M.J., Bayliss, R.D., Berry, F.J., and Greaves, C. (2011). The Synthesis, Structure, Magnetic and Electrical Properties of FeSb$_{2-x}$Pb$_x$O$_4$. J. Mater. Chem. 21, 14523–14529.

44. Chater, R., and Gavarri, J.R. (1985). Structure isomorphes MeX_2O$_4$ Evolution structural entre 2K et 300 K de l'antimonite FeSb$_2$O$_4$: Elasticite et ordre magnetique anisotropes. J. Solid State Chem. 60, 78–86.

45. Allen, J.P., Carey, J.J., Walsh, A., Scanlon, D.O., and Watson, G.W. (2013). Electronic Structures of Antimony Oxides. J. Phys. Chem. C 117, 14759–14769.

46. Saal, T., Christe, K.O., and Haiges, R. (2018). Lewis adduct formation of hydrogen cyanide and nitriles with arsenic and antimony pentafluoride. Dalton Trans. 48, 99–106.

47. Trofimov, V.G., Sheinkman, A.I., and Kleshchev, G.V. (1973). Antimony Pentoxide in the Crystalline State. J. Struct. Chem. 14, 245–248.

48. Andrews, J.L., Mukherjee, A., Yoo, H.D., Parija, A., Marley, P.M., Fakra, S., Prendergast, D., Cabana, J., Klie, R.F., and Banerjee, S. (2018). Reversible Mg-Ion Insertion in a Metastable One-Dimensional Polymorph of V$_2$O$_5$. Chem 4, 564–585.

49. Rong, Z., Malik, R., Canepa, P., Sai Gautam, G., Liu, M., Jain, A., Persson, K., and Ceder, G. (2015). Materials Design Rules for Multivalent Ion Mobility in Intercalation Structures. Chem. Mater. 27, 6016–6021.

50. Toby, B.H. (2001). EXPGUI, a Graphical User Interface for GSAS. J. Appl. Cryst. 34, 210–213.

51. Momma, K., and Izumi, F. (2008). VESTA: A Three-Dimensional Visualization System for Electronic and Structural Analysis. J. Appl. Cryst. 41, 653–658.

52. Ravel, B., and Newville, M. (2005). ATHENA, ARTEMIS, HEPHAESTUS: data analysis for X-ray absorption spectroscopy using IFEFFIT. J. Synchrotron Radiat. 12, 537–541.

53. Kresse, G., and Hafner, J. (1993). Ab initio molecular dynamics for open-shell transition metals. Phys. Rev. B Condens. Matter 48, 13115–13118.

54. Kresse, G., and Furthmüller, J. (1996). Efficiency of Ab-Initio Total Energy Calculations for Metals and Semiconductors Using a Plane-Wave Basis Set. Comput. Mater. Sci. 6, 15–50.

55. Blöchl, P.E. (1994). Projector augmented-wave method. Phys. Rev. B Condens. Matter 50, 17953–17979.

56. Joubert, D. (1999). From Ultrasoft Pseudopotentials to the Projector Augmented-Wave Method. Phys. Rev. B -. Condens. Matter Mater. Physiol. 59, 1758–1775.

57. Perdew, J.P., Burke, K., and Ernzerhof, M. (1996). Generalized Gradient Approximation Made Simple. Phys. Rev. Lett. 77, 3865–3868.

58. Jain, A., Hautier, G., Moore, C.J., Ping Ong, S., Fischer, C.C., Mueller, T., Persson, K.A., and Ceder, G.A. (2011). High-Throughput Infrastructure for Density Functional Theory Calculations. Comput. Mater. Sci. 50, 2295–2310.

59. Yu, M., and Trinkle, D.R. (2011). Accurate and efficient algorithm for Bader charge integration. J. Chem. Phys. *134*, 064111.

60. Stukowski, A. (2010). Visualization and Analysis of Atomistic Simulation Data with OVITO-the Open Visualization Tool. Model. Simul. Mater. Sci. Eng. *18*, 015012.

61. Henkelman, G., Uberuaga, B.P., and Jónsson, H. (2000). Climbing Image Nudged Elastic Band Method for Finding Saddle Points and Minimum Energy Paths. J. Chem. Phys. *113*, 9901–9904.

62. Okubo, M., Tanaka, Y., Zhou, H., Kudo, T., and Honma, I. (2009). Determination of activation energy for Li ion diffusion in electrodes. J. Phys. Chem. B *113*, 2840–2847.

63. Maintz, S., Deringer, V.L., Tchougréeff, A.L., and Dronskowski, R. (2016). LOBSTER: A tool to extract chemical bonding from plane-wave based DFT. J. Comput. Chem. *37*, 1030–1035.